Fig. 1).[1,2] The radiographic parameters we used for classification were ulnar translocation and carpal height ratio (Table 1).[1] In the current study, we also investigated our cases with or without scaphoid-lunate (S-L) dissociation (the gap between scaphoid and lunate is more than 2 mm[12] on the anteroposterior radiograph) in relation to the radiographic subtypes of RA.

Image Acquisition

The technique we used for *in vivo* 3-D kinematic evaluation has been described in detail previously.[14–19] For patients with RA, we performed 3-D CT on the wrists using a clinical helical type scanner with an image slice thickness of 0.625 mm (LightSpeed Ultra16; General Electric, Waukesha, WI). For the normal wrists of volunteers, magnetic resonance images were obtained using a 1.5-T commercial magnetic resonance imaging (MRI) system (Magnetom Vision PlusR 1.5T MRI; Siemens, Munich, Germany) in conjunction with a receive-only surface coil of 2.3 ms/33 ms, a flip angle of 45°, a 160-mm field of view, and 0.5-mm-thick contiguous slices, with 0.6 × 0.8 mm pixels. For each wrist, we acquired image with the wrist in 3 different positions: neutral (in which the third metacarpal and the forearm axis were aligned), maximum wrist flexion, and maximum wrist extension. For normal volunteers, we used a custom-made device to hold the position during image acquisition. However, we could not use the device for RA patients because of pain and deformity of the wrists. Data were saved in a standard format (Digital Imaging and Communications in Medicine [DICOM]) that is used commonly for transferring and storing medical images.

Segmentation and Construction of a 3-D Surface Bone Model

Segmentation was defined as extracting bone regions individually. The anatomic structure or region of interest must be delineated and separated so that it can be viewed individually and 3-D bone models can be reconstructed. Regions of individual bones were segmented semiautomatically using a software program for image analysis (Virtual Place-M; AZE, Ltd., Tokyo, Japan). The software generated 3-D surface bone models using the marching cubes technique.[14,15,20]

Registration

We created 3-D bone models and quantitatively evaluated the motion of the midcarpal joint using a markerless volume-based registration technique. The kinematic variables were calculated by registering the bone, obtained by segmentation, from one position to another. The accuracy of volume-based registration has been discussed previously,[14,15] the mean rotation error was 1° ± 1, and the mean translation error was 0.21 mm ± 0.25.

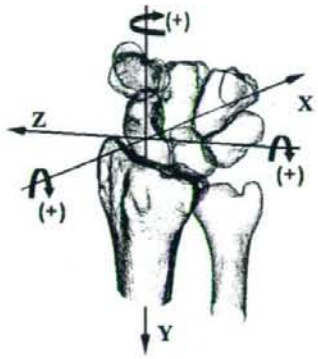

FIGURE 2: A consistent orthogonal reference system established in the radius.

Three-Dimensional Quantification of the Range of Motion

To quantify the 3-D range of motion of the midcarpal joint, we defined the grid for the radius, which was the orthogonal reference system advocated by Belsole et al (Fig. 2).[15,21,22] The total amount of wrist motion in the flexion-extension plane was defined as the total range of motion of the radiocarpal and midcarpal joint in the flexion-extension plane, which was evaluated by assessing the range of capitate motion relative to the reference system established on the radius. The range of radiocarpal motion in the flexion-extension plane was investigated by that of the lunate motion. Then the range of the midcarpal motion in the flexion-extension plane could be quantified as the difference between the total amount of wrist motion and the range of radiocarpal motion.

In the flexion-extension motion of the wrist, the radiocarpal and midcarpal joints have motions in planes other than the flexion-extension plane such as the pronation/supination (P/S) plane and the radial/ulnar deviation (RD/UD) plane. There are coupling motions associated with wrist motion in the flexion-extension plane. We defined the 2 motions in the other planes as *out of the plane motion (P/S)* and *out of the plane motion (RD/UD)*, respectively. We quantified the amount of wrist motion in the flexion-extension plane and out of the plane separately for the radiocarpal and midcarpal joints.

A consistent orthogonal reference system was established in the radius as follows.[22] The y axis was defined as the longitudinal radial axis and indicated the proximal (+)/distal (–) direction. The z axis was defined as the line running through the styloid process on the plane perpendicular to the y axis and indicated the radial (+)/ulnar (–) direction. The x axis was defined as the line perpendicular to the yz plane and indicated the palmar (+)/dorsal (–) direction. Rotation around the z axis produced flexion (+)/extension (–), rotation around the y axis was pronation (+)/supination (–), and rotation around the x axis was ulnar (+)/radial (–)

deviation (Fig. 2). We defined the rotating angle of the carpus around each of the 3 axes as the range of wrist motion.

Evaluation of the Contribution Ratio

We also evaluated the individual contributions of radiocarpal and midcarpal motion to the total amount of wrist motion. We defined *contribution ratio* as the percentage of the range of radiocarpal motion or midcarpal motion relative to the total amount of wrist motion. In this study, the contribution ratio was investigated only in the flexion-extension plane.

Statistical Analysis

All data were expressed as the mean with the standard deviation. Quantitative comparison of results between the control group and the RA group was performed using standard statistical formulas based on the Mann-Whitney U test. Results were deemed to be significant if $p < .05$.

RESULTS

Rheumatoid Arthritis Versus Normal

In the rheumatoid wrists, the average of total amount of wrist motion in the flexion-extension plane was 59° ± 20. The average range of radiocarpal motion in the flexion-extension plane was 27° ± 15 and that of midcarpal motion was 32° ± 17. In the normal wrists, the average of total amount of wrist motion in the flexion-extension plane was 111° ± 15. The average range of radiocarpal motion in the flexion-extension plane was 63° ± 14° and that of midcarpal motion was 47° ± 8. The ranges of radiocarpal motion ($p < .01$) and midcarpal motion ($p < .01$) in the flexion-extension plane in RA wrists were significantly less than normal as expected (Table 2). The average contribution ratios of radiocarpal and midcarpal joint in the flexion-extension plane were 46% and 54%, respectively, in RA wrists and 57% and 43%, respectively, in normal wrists (Fig. 3). On average, the midcarpal joint tended to have a greater contribution in the flexion-extension plane in RA wrists compared with normal wrists, even though the difference was not significant ($p = .179$).

Regarding the out of the plane motion of the wrists, the average of total amount of out of the plane motion (P/S) in RA was 8° ± 11 in supination during flexion motion of the wrist. The average range of out of the plane motion (P/S) in the radiocarpal joint was 5° ± 7 and that in the midcarpal joint was 2° ± 8 in supination during flexion motion of the wrists. In the normal wrists, the average of total amount of out of the plane motion (P/S) was 8° ± 13 in pronation during flexion motion of the wrists. The average range of out of the plane motion (P/S) in the radiocarpal joint was 3° ± 6 and that in the midcarpal joint was 4° ± 9 in pronation during flexion motion of the wrists. Consequently, during flexion motion of the wrists, the radiocarpal joint ($p < .01$) and the whole wrist joint, that is, the total for the radiocarpal and midcarpal joints ($p < .01$), significantly supinated in RA wrists compared with normal (Table 2).

The average of total amount of out of the plane motion (RD/UD) in RA was 5° ± 8 in ulnar deviation during flexion motion of the wrists. The average of out of the plane motion (RD/UD) in the radiocarpal joint was 1° ± 7 and that in the midcarpal joint was 4° ± 8 in ulnar deviation during flexion motion of the wrists. In the normal wrists, the average of total amount of out of the plane motion (RD/UD) was 8° ± 13 in radial deviation during flexion motion of the wrists. The average range of out of the plane motion (RD/UD) in the radiocarpal joint was 4° ± 8 and that in the midcarpal joint was 4° ± 8 in radial deviation during flexion motion of the wrists. Consequently, during flexion motion of the wrists, the midcarpal joint ($p < .05$) and the whole wrist joint, that is, the total for the radiocarpal and midcarpal joints ($p < .01$), significantly deviated ulnarly in RA wrists compared with normal (Table 2).

Stable Form Versus Unstable Form of RA

We classified the 30 rheumatoid wrists into 19 cases of stable form of disease and 11 cases of unstable form. The average of total ulnar translocation after onset of RA was 4.1 mm in the stable form and 10.7 mm in the unstable form; these values are consistent with the radiographic parameters described by Simmen and Huber (Table 1).[1] The average of total loss of carpal height ratio after onset of RA was 0.12 in the stable form and 0.28 in the unstable form; these values are also consistent with the radiographic parameters described by Simmen and Huber (Table 1).[1] Among the 11 wrists in the unstable form of disease, 7 showed S-L dissociation. In contrast, S-L dissociation was not found among the 19 wrists in the stable form of disease.

The range of radiocarpal and midcarpal motions in the flexion-extension plane varied greatly among cases in the stable form of disease (Fig. 4). In contrast, the range in cases of the unstable form was relatively constant; in 8 of the 11 wrists in unstable form, the midcarpal motion in the flexion-extension plane was greater than radiocarpal motion (Figs. 4, 5). Only 3 cases of the unstable form had greater motion in the radiocarpal joint than in the midcarpal joint (Fig. 4). The average ranges of radiocarpal and midcarpal motion in the flexion-extension plane were 31° ± 16 and 28° ± 15, respectively, in the stable form, and 20° ± 12 and 38° ± 19, respectively, in the unstable form. In the radiocarpal joint, the range of motion of the unstable form in the flexion-extension plane was significantly less than that of the stable form ($p < .05$), whereas in the midcarpal joint, there was no significant difference ($p < .05$) between the 2 groups (Table 3). The average contribution ratios of radiocarpal and midcarpal joint in the flexion-extension plane were 53% and 47%, respectively, in the stable form and 33% and 67%, respectively, in the unstable form (Fig. 6). In the midcarpal joint, the contribution ratio of the unstable-form group in the flexion-extension plane was significantly greater than that of the stable-form group ($p < .05$).

Regarding out of the plane motion (P/S) of the rheumatoid wrists, during flexion motion of the wrists, the

TABLE 2: Kinematic Data During Flexion Motion of the Wrist: RA Versus Normal Wrists

	Range of Motion During the Flexion Motion of the Wrists (°)								
	In the Flexion-Extension Plane Motion			Out of the Flexion-Extension Plane Motion					
	Flexion (+)/Extension (–)			Pronation (+)/Supination (–)			Ulnar (+)/Radial (–) Deviation		
	Radiocarpal Motion	Midcarpal Motion	Total Amount of Motion	Radiocarpal Motion	Midcarpal Motion	Total Amount of Motion	Radiocarpal Motion	Midcarpal Motion	Total Amount of Motion
Normal (n = 10)									
Average	63	47	111	3	4	8	–4	–4	–8
SD	14	8	15	6	9	13	8	8	13
RA (n = 30)									
Average	27**	32**	59**	–5**	–2	–8**	1	4*	5**
SD	15	17	20	7	8	11	7	8	8

*p < .05, **p < .01 versus normal.

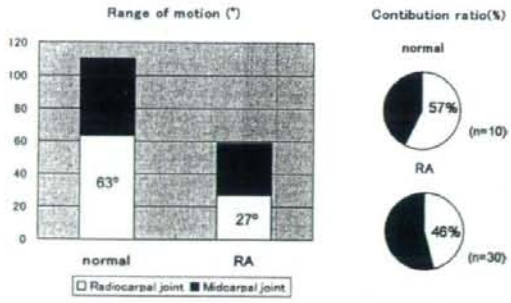

FIGURE 3: Average range of motion and contribution ratios of the radiocarpal and midcarpal joint in the flexion-extension plane in normal and RA wrists. The contribution ratio is the percentage contribution of radiocarpal or midcarpal motion relative to the total amount of wrist motion.

FIGURE 5: Flexion-extension motions of the lunate and capitate relative to the radius in the stable and unstable forms of RA wrists, viewed from the ulnar side. **A** Representative case of the stable form of RA, shown in Figure 1A, in which the range of motion in the flexion-extension plane was 40° in the radiocarpal joint and 5° in the midcarpal joint (Video 1, a 3-dimensional animation of a representative case of the stable form of RA wrist, may be viewed at the *Journal's* Web site, www.jhandsurg.org). **B** Representative case of the unstable form of RA, shown in Figure 1B, in which the range of motion in the flexion-extension plane was 37° in the radiocarpal joint and 83° in the midcarpal joint (Video 2, a 3-dimensional animation of a representative case of the unstable form of RA wrist, may be viewed at the *Journal's* Web site, www.jhandsurg.org).

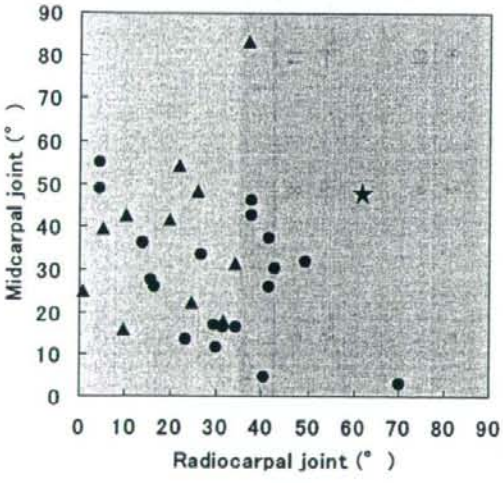

FIGURE 4: Scattering diagram of the range of the radiocarpal and midcarpal motion in the flexion-extension plane in stable and unstable forms of RA wrists and in normal wrists: ●, stable form of RA (19 cases); ▲, unstable form of RA (11 cases); ★, average range of motion in 10 normal wrists (63° in the radiocarpal joint and 47° in the midcarpal joint).

midcarpal joint ($p < .05$) and the whole wrist joint, that is, the total for the radiocarpal and midcarpal joints ($p < .01$), significantly supinated in the unstable-form group compared with the stable-form group. Regarding out of the plane motion (RD/UD), we found no significant difference ($p < .05$) between the 2 groups (Table 3).

DISCUSSION

Kinematic evaluation of rheumatoid wrists by x-ray has been difficult because of the complicated and overlapping shapes of the carpal bones. In the current study, we quantitatively evaluated the amount of radiocarpal and midcarpal motion in the flexion-extension plane of the rheumatoid wrists using 3-D CT. We also elucidated the relationship between the contribution of midcarpal motion to the total amount of wrist motion in the flexion-extension plane and the radiographic subtypes of RA.

We found that the contribution of midcarpal motion to the total amount of wrist motion in the flexion-extension plane was significantly greater in the unstable form than in the stable form of RA (Table 3 and Fig. 6). This result may seem counterintuitive because of the radiographic appearance of the unstable form of RA in which all parts of the wrist joints are severely damaged. We speculate that our results can be accounted for mainly by stronger skeletal constraints in the midcarpal joint than in the radiocarpal joint. The midcarpal joint has its own self-stabilizing mechanism; when the trapezium is axially loaded against the scaphoid, the flexion moment by the scaphoid is constrained by the extension moment experienced by the triquetrum, and stable equilibrium is achieved.[19] Moreover, the midcarpal joint is proved to have an adaptive mechanism whereby the concave and convex joint surfaces allow preservation of articular congruity.[19] On the other hand, the stability of the radiocarpal joint depends on ligamentous constraints. In the radiocarpal joint, the carpal bones tend to slide ulno-palmarward on the sloping plane of the distal radius, and the displacement is resisted by the palmar and dorsal radiotriquetral and palmar RL ligaments.[22] It is likely that the radiocarpal joint in which joint stability depends on ligamentous constraints easily loses its stability, particularly in the unstable form of RA.

Scapholunate dissociation can be associated with RA wrist by the multiple laxities of ligaments including the dorsal scapholunate ligament, especially in the unstable form of RA. In the current study, S-L dissociation occurred in 7 of 11 wrists in the unstable form of RA; however, it did not occur in any of the 19 wrists in the stable form. This may have the relationship to our results that the range of

TABLE 3: Kinematic Data During Flexion Motion of the Wrist: Stable Versus Unstable Forms of RA

	Range of Motion During the Flexion Motion of the Rheumatoid Wrists (°)								
	In the Flexion-Extension Plane Motion			Out of the Flexion-Extension Plane Motion					
	Flexion (+)/Extension (–)			Pronation (+)/Supination (–)			Ulnar (+)/Radial (–) Deviation		
	Radiocarpal Motion	Midcarpal Motion	Total Amount of Motion	Radiocarpal Motion	Midcarpal Motion	Total Amount of Motion	Radiocarpal Motion	Midcarpal Motion	Total Amount of Motion
Stable form (n = 19)									
Average	31	28	59	–3	0	–3	2	3	5
SD	16	15	15	5	7	9	5	7	7
Unstable form (n = 11)									
Average	20*	38	58	–9	–7*	–16**	1	6	7
SD	12	19	25	9	7	10	8	9	9

*p < .05, **p < .01 versus stable form.

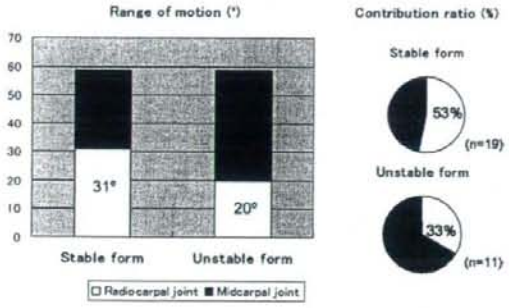

FIGURE 6: Average range of motion and the contribution ratios of the radiocarpal and midcarpal joints in the flexion-extension plane in the stable and unstable forms of RA wrists. The contribution ratio is the percentage of the contribution of the radiocarpal motion or midcarpal motion relative to the total amount of wrist motion.

radiocarpal motion in the unstable form in the flexion-extension plane was significantly less than that in the stable form. In the normal wrists, if the interosseous ligament between scaphoid and lunate is disrupted, the scaphoid tends to flex and the lunate tends to extend and the congruity of the radiocarpal joint is lost.[23] These tendencies may lead to the loss of the range of radiocarpal motion.

Regarding the motion of the wrists outside the flexion-extension plane, we found RA wrists significantly deviated ulnarly during flexion motion compared with normal (Table 2). This may be related to the unique motion patterns of the midcarpal joint. It has been reported that the essential plane of motion of the midcarpal joint is oblique to the anatomic planes, which corresponds with extension with radial deviation and flexion with ulnar deviation—the so-called dart-throwing motion.[19] Under the severe destruction of the radiocarpal joint in RA, especially in the unstable form, it is possible that the preserved midcarpal function facilitates the dart-throwing motion rather than the pure flexion-extension motion. This dart-throwing motion seems to be helpful for patients with RA because the oblique motion is used in performing many tasks of daily living such as hair combing, washcloth wringing, shoe tying, and can-opening.[24,25]

Most clinical reports have asserted that osseous procedures such as partial fusions of compartments of the joint are recommended to stabilize wrists with RA.[1] It has been suggested that RL arthrodesis is indicated only in the middle stage of the osteoarthritis type of RA and that other types such as the unstable form of RA may be better treated by total wrist arthrodesis.[3] However, reconsideration is needed because total wrist arthrodesis involves considerable loss of wrist function. Borisch and Haussmann[10] reported that the RL arthrodesis was able to reestablish the midcarpal joint and that the carpus showed an amazing capacity of adaptation. Ishikawa et al[11] suggested that radiocarpal fusion resulted in good stability with preservation of motion despite radiographic progression of the disease. Our results showing that the midcarpal motion in the unstable form of RA was better preserved than previously thought may support more positive application of RL arthrodesis in certain cases with the unstable form of RA. However, our results do not predict wrist function perfectly after RL arthrodesis in ongoing disease, because previous researchers reported that although the midcarpal joint space was generally preserved after radiocarpal arthrodesis, some wrists lost the joint space and became stiff.[9,11]

The current study has some limitations. The most important limitation is that we compared data on patients with RA based on CT images with data on normal volunteers based on MRI. However, we quantified the range of joint motion as the rotational angle of the carpus relative to a reference system established in the radius. The way in which the images are acquired may not affect the overall results if it is under the accuracy of volume-based registration. A second limitation of this study is that the patients with RA wrists were not fully matched for age and gender with the normal-wrist volunteers. The results might have been different if these demographic parameters of the study groups were identical. A further limitation is that during image acquisition, we were unable to use the position-holding device in the RA patients to maintain the neutral, maximum flexion, and extension positions because of symptomatic pain and wrist deformity. Because the patients used their own muscle power to hold their wrists in position, the positions recorded may not have been precisely maximum flexion and maximum extension.

Nevertheless, the results of this study may be useful in establishing a treatment plan in advanced cases of RA. Even some cases in the stable form of RA wrist may be treated by RL fusion, particularly the cases in which the midcarpal joint space is not visible on x-ray but the midcarpal motion is preserved under the 3-D investigation. Based on our findings of the preservation of a great amount of motion at the midcarpal joint in rheumatoid patients with symptomatic wrists, we believe that our study rationally supports the application of RL arthrodesis rather than total wrist arthrodesis as treatment in appropriate RA patients.

REFERENCES

1. Simmen BR, Huber H. The rheumatoid wrist: a new classification related to the type of the natural course and its consequences for surgical therapy. In: Simmen BR, Hagena FW, eds. The wrist in rheumatoid arthritis. Rheumatology. Basel: Karger, 1992:13–25.
2. Flury MP, Herren DB, Simmen BR. Rheumatoid arthritis of the wrist. Classification related to the natural course. Clin Orthop 1999;366:72–77.
3. Della Santa D, Chamay A. Radiological evolution of the rheumatoid wrist after radio-lunate arthrodesis. J Hand Surg 1995;20B:146–154.
4. Chamay A, Della Santa D, Vilaseca A. Radiolunate arthrodesis. Factor of stability for the rheumatoid wrist. Ann Chir Main 1983;2:5–17.
5. Linscheid RL, Dobyns JH. Radiolunate arthrodesis. J Hand Surg 1985;10A:821–829.

6.Stanley JK, Boot DA. Radiolunate arthrodesis. J Hand Surg 1989;14B:283–287.
7.Ishikawa H, Hanyu T, Saito H, Takahashi H. Limited arthrodesis for the rheumatoid wrist. J Hand Surg 1992;17A: 1103–1109.
8.Halikis MN, Colello-Abraham K, Taleisnik J. Radiolunate fusion. The forgotten partial arthrodesis. Clin Orthop 1997; 341:30–35.
9.Doets HC, Raven EEJ. Radiolunate arthrodesis. A procedure for stabilizing and preserving mobility in the arthritic wrist. J Bone Joint Surg 1999;81B:1013–1016.
10.Borisch N, Haussmann P. Radiolunate arthrodesis in the rheumatoid wrist: a retrospective clinical and radiological long-term follow-up. J Hand Surg 2002;27B:61–72.
11.Ishikawa H, Murasawa A, Nakazono K. Long-term follow-up study of radiocarpal arthrodesis for the rheumatoid wrist. J Hand Surg 2005;30A:658–666.
12.Muramatsu K, Ihara K, Tanaka H, Kawai S. Carpal instability in rheumatoid wrists. Rheumatol Int 2004;24:34–36.
13.Besl PJ, Mackay N. A method for registration of 3-D shapes. IEEE Trans Pattern Anal 1992;14:239–256.
14.Goto A, Moritomo H, Murase T, Oka K, Sugamoto K, Arimura T, et al. In vivo three-dimensional wrist motion analysis using magnetic resonance imaging and volume-based registration. J Orthop Res 2005;23:750–756.
15.Oka K, Moritomo H, Murase T, Goto A, Sugamoto K, Yoshikawa H. Patterns of carpal deformity in scaphoid nonunion: a three-dimensional and quantitative analysis. J Hand Surg 2005;30A:1136–1144.
16.Oka K, Doi K, Suzuki K, Murase T, Goto A, Yoshikawa H, et al. In vivo three-dimensional motion analysis of the forearm with radioulnar synostosis treated by the Kanaya procedure. J Orthop Res 2006;24:1028–1035.
17.Moritomo H, Goto A, Sato Y, Sugamoto K, Murase T, Yoshikawa H. The triquetrum-hamate joint: an anatomic and in vivo three-dimensional kinematic study. J Hand Surg 2003;28A:797–805.
18.Moritomo H, Murase T, Goto A, Oka K, Sugamoto K, Yoshikawa H. Capitate-based kinematics of the midcarpal joint during wrist radioulnar deviation: an in vivo three-dimensional motion analysis. J Hand Surg 2004;29A:668–675.
19.Moritomo H, Murase T, Goto A, Oka K, Sugamoto K, Yoshikawa H. In vivo three-dimensional kinematics of the midcarpal joint of the wrist. J Bone Joint Surg 2006;88A: 611–621.
20.Lorensen WE, Cline HE. Marching cubes: a high resolution 3D surface construction algorithm. Computer Graphics 1987;21:163–169.
21.Belsole RJ, Hilbelink DR, Llewellyn JA, Dale M, Ogden JA. Carpal orientation from computed reference axes. J Hand Surg 1991;16A:82–90.
22.Arimitsu S, Murase T, Hashimoto J, Oka K, Sugamoto K, Yoshikawa H, et al. A three-dimensional quantitative analysis of carpal deformity in rheumatoid wrists. J Bone Joint Surg 2007;89B:490–494.
23.Linscheid RL, Dobyns JH, Beckenbaugh RD, Cooney WP, Wood MB. Instability patterns of the wrist. J Hand Surg 1983;8:682–686.
24.Li ZM, Kuxhaus L, Fisk JA, Christophel TH. Coupling between wrist flexion-extension and radial-ulnar deviation. Clin Biomech (Bristol, Avon) 2005;20:177–183.
25.Palmer AK, Werner FW, Murphy D, Glisson R. Functional wrist motion: a biomechanical study. J Hand Surg 1985;10A: 39–46.

Clin Rheumatol (2008) 27:733–737
DOI 10.1007/s10067-007-0781-0

ORIGINAL ARTICLE

Radiological study of joint destruction patterns in rheumatoid flatfoot

Takako Hattori · Jun Hashimoto · Tetsuya Tomita · Takashi Kitamura · Hideki Yoshikawa · Kazuomi Sugamoto

Received: 15 January 2007 / Revised: 9 October 2007 / Accepted: 14 October 2007 / Published online: 20 November 2007

Abstract The purpose of this study was to clarify variations in patterns of flattening in rheumatoid hindfoot. Out of 232 outpatients with rheumatoid arthritis treated at our hospital from 2001 to 2003, we studied lateral radiographs of feet of 216 patients (423 weight-bearing views). We measured the medial arch angle (MAA) and talar angle (TA) and compared the alignment of the talonavicular joint–sagittal plane of each foot. We also evaluated the relationship between the severity of flattening and inclination of the talus and performed cluster analysis. Three groups were clustered by MAA and TA. In group I, joints were normal or close to normal. In group II, both talonavicular and subtalar joints were affected. In group III, talonavicular joints were minimally affected, and the subtalar joints were primarily affected. Groups II and III were thought to be a different pattern of flattening. The present results suggest that there are at least two patterns of flattening in rheumatoid hindfoot.

Keywords Flatfoot · Hindfoot · Radiography · Rheumatoid arthritis

T. Hattori (✉) · J. Hashimoto · T. Tomita · H. Yoshikawa · K. Sugamoto
Department of Orthopedic Surgery,
Osaka University Medical School,
2-2, Yamadaoka,
Suita, Osaka 565-0871, Japan
e-mail: takatin@alpha-net.ne.jp

T. Kitamura
Department of Orthopedic Surgery,
Sumitomo Hospital,
5-3-20, Nakanoshima, Kita,
Osaka, Osaka 530-0005, Japan

Introduction

Rheumatoid arthritis (RA) causes numerous joint disorders and is associated with a high incidence of foot lesions. Approximately 90% of RA patients exhibit positive radiological changes in the foot [1, 2]. In a study by Vidigal et al. [3], radiological examination revealed that 26% of the RA patients had disorders of the ankle and that 32% had subtalar joint disorders [11]. In a study by Resnick and Niwayama [4, 5], the subtalar joint was affected in 29% of the RA patients, the talocalcaneonavicular joint was affected in 39%, and the calcaneocuboid joint was affected in 25%. In a study by Spiegel and Spiegel [6], 25% of the patients who had had RA for >5 years had an abnormal hindfoot valgus on weight-bearing. Reports indicate that pes planovalgus is a common feature of rheumatoid hindfoot deformity in RA patients [1, 7, 8]. In rheumatoid hindfoot deformity, soft tissue inflammation occurs under weight-bearing conditions in the hindfoot joints, with subsequent loss of articular cartilage, erosion of the talonavicular and subtalar joints, and possible posterior tibial tendon dysfunction. This causes the talar head to fall downwards towards the medial side of the foot in the planter direction, and causes the calcaneus to drift into the valgus, leading to pes planovalgus deformity of the hindfoot [9–11].

It is unclear how duration of RA is related to the type and severity of displacement of each part of the foot. There have been no reported studies of the types of flatfoot deformities. During daily clinical imaging, we see patients who have flatfeet with severe valgus deformities or highly flattened feet without valgus. Consequently, we hypothesize that flatfoot deformity occurs in several different forms.

In the present large-scale radiographic study, we sought to determine whether there are variations in rheumatoid flatfoot deformity.

Materials and methods

We examined standard X-rays of ankle joints obtained from 2001 to 2003 from 232 patients who satisfied the American College of Rheumatology criteria for RA [12]. We excluded 41 feet from the present study due to previous arthrodesis or ankle joint replacement (30 feet), or because the X-rays were unreadable (11 feet). The remaining 216 RA patients (423 feet) were included in the present study, including 26 patients (34 feet) who had undergone forefoot operations, e.g., metatarsal decapitation or MTP arthrodesis. The subjects comprised 28 men and 188 women, with an age range of 23 to 84 years (mean, 57.0 years). We did not assess the history of drug administration, including steroids, or the duration of RA.

Radiographic procedure

Lateral X-ray images of bilateral ankle joints were obtained from each patient at the time of final examination. X-rays were then taken in the weight-bearing position. The patient was instructed to stand on one foot, on a platform that was several centimeters high. The incidence ray was perpendicular to the center of the Chopart joint. The horizontal image included the entire foot from heel to toes.

Measurements

Radiographic measurements were performed on the basis of standard X-ray views. We studied the radiographs of each foot and measured the following three items.

Medial arch angle

According to the criteria of Bouysset et al. [10, 13–15], flatfoot is defined as a medial arch angle (MAA) of >130° (Fig. 1a). In Bouysset's method [10, 13, 14], the MAA is formed by the intersection of two lines. The first line extends from the lowest point of the sesamoid to the lowest point of the talonavicular joint. The second line is formed by aligning the first line with the lowest point of the calcaneus. We classified feet into the following three groups: MAA<118° (MAA<118° group); 118°≤MAA<130° (118°≤MAA<130° group); MAA>130° (MAA>130° group). A fourth group, the MAA<130° group, was created by combining the MAA<118° and 118°≤MAA<130° groups.

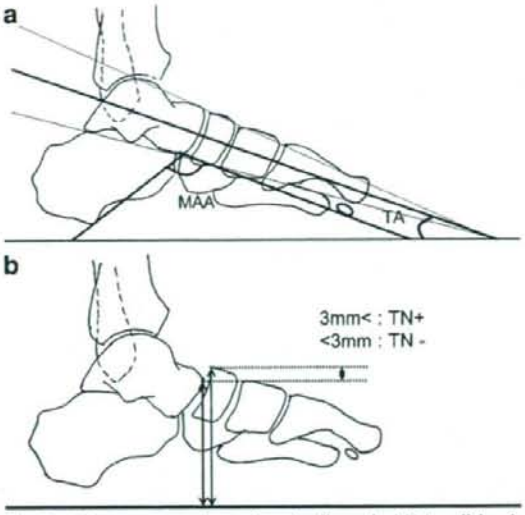

Fig. 1 **a** Measurement angles on lateral radiograph: *MAA* medial arch angle, *TA* talar angle. **b** TN+ indicates that the difference between the lengths of the two perpendiculars is ≥3 mm. TN− indicates that the difference is <3 mm. The first line extends from the distal upper edge of talus to the floor, and the second line runs from the proximal edge of the navicular

Talar angle

The talar angle (TA) is the angle between the axis of the talus and the horizontal plane created by contact between the foot and the floor. The axis of the talus was determined using Tomeno's method [10, 13, 16]: The tangents of the upper and lower surfaces of the talus form an angle; the bisector of this angle is the axis of the talus.

Alignment of talonavicular joint–sagittal plane (TN)

To determine the alignment of the talonavicular joint, a vertical line is drawn from the distal upper edge of the talus to the floor, and vertical line is drawn from the proximal upper edge of the navicular to the floor (Fig. 1b). Based on the difference in length between these two vertical lines, we classified the feet into two categories: (1) difference in length ≥3 mm (TN+ group); (2) difference in length <3 mm (TN− group).

Statistical analysis

Data were analyzed using the analytical software JMP IN 5.1. We performed *t* tests to assess the significance of differences in average MAA and TA values between the MAA<130° and MAA>130° groups. We performed hierarchical cluster analysis with Euclidean distance using

the Ward method, to determine whether the participants could be divided into groups based on a combination of MAA and TA. To assess the significance of differences between the TN+ and TN− groups, we performed the F test and χ^2 test as appropriate.

Results

Medial arch angle

The measured MAA values ranged from 90° to 158° (mean± SD, 128°±10.35; Table 1). The MAA<118° group comprised 55 feet (13%); the 118°≤MAA<130° group comprised 198 feet (47%); and the MAA>130° group comprised 170 feet (40%).

Talar angle

The measured TA values ranged from 8° to 58° (mean±SD, 29°±7.15).

Alignment of talonavicular joint–sagittal plane

The TN+ group comprised 70 feet (16.5%), and the TN− group comprised 353 feet (83.5%).

Correlation between MAA and TA

The scatter plot with TA on the y-axis and MAA on the x-axis is shown in Fig. 2. There was a statistically significant correlation between MAA and TA (r=0.448). The mean TA of the MAA>130° group was 33.0°. The mean TA of the MAA<130° group was 27.0°. TA was significantly greater for the MAA>130° group than for the MAA<130° group (p<0.0001). Within the MAA>130° group, there was no statistically significant correlation between MAA and TA (r=0.1453; Fig. 3).

Table 1 Type of deformation by medial arch angle, mean of the talar angle, and talonavicular instability numbers

Type of deformation	TA mean angle	TN+ Number	TN−
MAA<118°	24.2° (8–37)	n=55 (13%)	
		1	54
118°<MAA<130°	27.74° (13–50)	n=198 (47%)	
		17	181
130°<MAA	33.03° (17–58)	n=170 (40%)	
		52	118

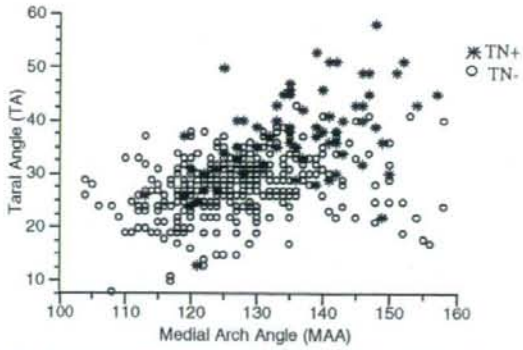

Fig. 2 Scatter diagram of all feet. MAA correlates slightly with TA (r=0.4477)

Correlation between MAA and TN

In the MAA>130° group, there were 52 TN+ feet and 118 TN− feet. In the MAA<130° group, there were 18 TN+ feet and 235 TN− feet. The chi-square test indicated that there was a significant difference in the frequency of TN+ feet between the MAA<130° and MAA>130° groups (p<0.0001).

Cluster analysis

As a result of the cluster analysis, the patients were divided into three groups: groups I, II, and III (Fig. 4). During clustering, one outlier (TA, 8°; MAA, 108°) was eliminated.

Group I comprised 273 feet (64.5%) and had the following characteristics: average MAA, 122°; average TA, 26.9°; 16 feet were TN+; 157 feet were TN−. Group II comprised 33 feet (7.8%) and had the following characteristics: average MAA, 143°; average TA, 45°; 27 feet were TN+; 5 feet were TN−. Group III comprised 116 feet (27.4%) and had the following characteristics: average

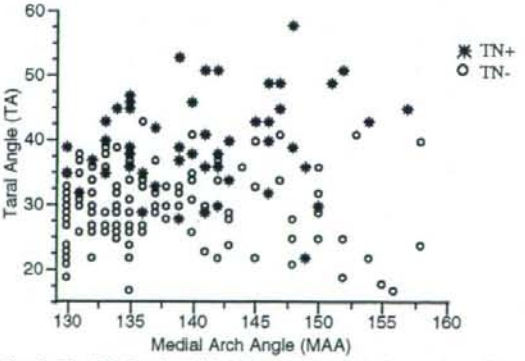

Fig. 3 The 170 feet in which MAA>130°. MAA does not correlate closely with TA (r=0.1453)

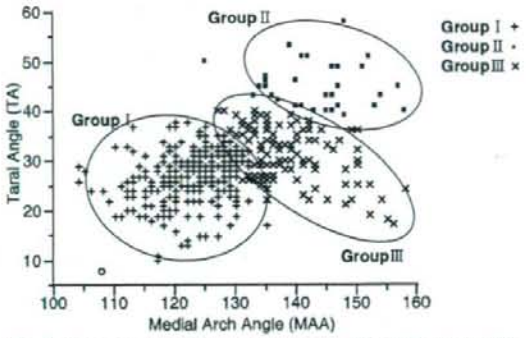

Fig. 4 Cluster analysis produced three groups. The *white circle at the lower left* was eliminated as an outlier. Group I is close to normal feet. Group II represents increased MAA and TA. In group III, MAA is increased, but TA is not generally increased

MAA, 138°; average TA, 31.2°; 27 feet were TN+; 89 feet were TN−. There were statistically significant differences in MAA, TA, and TN between groups I, II, and III (Table 2).

Discussion

Generally, flatfoot is related to a decrease in the length of the longitudinal arch. The measurements commonly used to evaluate flatfoot include the calcaneal pitch, TA, MAA, and first metatarsal pitch [17, 18]. When Bouysset et al. measured the internal arch angle (MAA), TA, and calcaneal angle of 397 RA feet, they found no significant difference in the calcaneal angle between patients with and without pain. That indicates that in flatfoot, the calcaneus is not flattened in the lateral X-ray view [10]. Therefore, in the present study, we defined MAA and TA according to the criteria of Bouysset et al., and we examined the alignment of the talonavicular joint.

In the abovementioned study by Bouysset et al., 15.4% of feet had an MAA of <118°, 58.9% of feet had an MAA of ≥118° and <130°, and 25.7% of feet had an MAA of >130°

Table 2 Intergroup data analysis

	Group I (n=273)	Group II (n=33)	Group III (n=116)	Test for group difference (p value)
MAA (mean angle±SD)	122± 5.97	143± 7.60	138±6.62	F=356.11 p<0.0001
TA (mean angle±SD)	26.9± 5.06	45.0± 4.57	31.2±5.45	F=191.14 p<0.0001
TN+ (feet)	16	27	27	p<0.0001
TN− (feet)	257	5	89	

Statistically significant differences in the three groups were observed. MAA and TA were analyzed by F test, and TN was analyzed by χ^2 test.

[10]. In the present study, 40% of feet had an MAA of >130°; this is a higher proportion of flatfoot than in the abovementioned study by Bouysset et al. In a study by Spiegel and Spiegel [6], flattening of the longitudinal and horizontal arch was observed in 46% of the patients with RA. The present results are consistent with these previous findings.

The most severe radiological changes in hindfoot joints occur as the joint space narrows and erosion occurs in the talonavicular joint. Changes also occur in the subtalar joint and the calcaneocuboid joint [7, 13]. Tibialis posterior tendon dysfunction or tears contribute to pes planovalgus deformity of RA feet [19, 20]. It is thought that these displacements in RA feet cause the head of the talus to fall downwards towards the medial side of the foot, cause the calcaneus to drift into valgus pronation, and cause subsidence of the navicular.

In the present large-scale study, in which we measured MAA, TA, and TN, we did not find a correlation between MAA and TA in cases of flatfoot (MAA>130°; r=0.1463), but we found a significant overall correlation between MAA and TA (r=0.4477). This indicates that the severity of flatfoot does not correlate with the extent of dislocation of the talus. This suggests that the talar head does not necessarily fall down in serious flatfoot, and that there are distinctly different patterns of deformation. Using cluster analysis, we classified the present subjects into three groups (groups I, II, and III) based on a combination of MAA and TA. We found that there are various patterns of deformation in RA flatfoot. Group I was closest to normal feet with minimal-to-no dislocation. Group II represents plantar dislocation of the talar head and subluxation of the

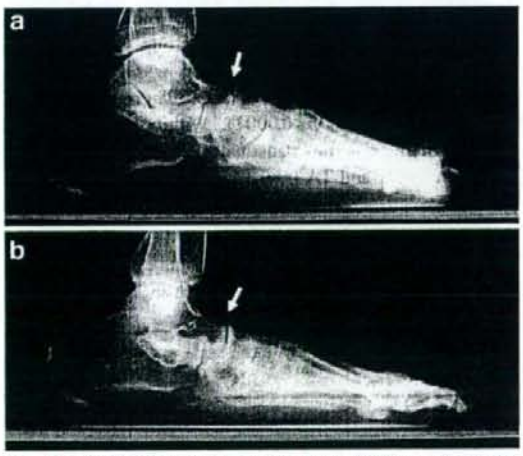

Fig. 5 Rheumatoid arthritis, lateral weight-bearing radiographs. **a** Group II: The image shows planter flexion of talar head and instability of talonavicular joint. **b** Group III: The image shows that the talonavicular joint is minimally affected, and shows instability of subtalar joint

talonavicular joint; both the subtalar and talonavicular joint are affected. In group III, the talonavicular joint was not generally affected, but the subtalar joint was primarily affected. This indicates that the feet in group III were flattened without destruction of the talonavicular joints (Fig. 5). Groups II and III appear to involve different patterns of flattening.

To examine valgus deformity in terms of rheumatoid flatfoot, we evaluated horizontal displacement of the calcaneus. However, we did not evaluate anteroposterior X-ray images of the calcaneus, and we did not evaluate horizontal displacement of the navicular to talar head, because the angle measurement in the frontal view of the ankle joint was not reliable. Accurate examination of valgus deformity may require three-dimensional evaluation with computed tomography (CT) and magnetic resonance imaging (MRI). However, because we believe that CT and MRI are impractical for a large-scale study of such deformation patterns, we used lateral X-ray images. Even with evaluation of only two parameters (tilting of the talus and alignment of talonavicular joint), we clearly identified deformation patterns. In addition, we preferred to focus our research on the extent of disorders in the talonavicular, subtalar, and calcaneocuboid joints.

The present results are also useful for choosing treatment methods, and for the choice of surgical intervention based on the pattern of joint destruction.

Conclusion

There are at least two distinct types of deformation of rheumatoid flatfoot. The present results are important for evaluating deformation in such cases, and are useful for choosing treatment options.

References

1. Vainio K (1956) The rheumatoid foot; a clinical study with pathological and roentgenological comments. Ann Chir Gynaecol Fenn Suppl 45:1–107
2. Thould AK, Simon G (1966) Assessment of radiological changes in the hands and feet in rheumatoid arthritis. Ann Rheum Dis 25:220–228
3. Vidigal E, Jacoby RK, Dixon AS et al (1975) The foot in chronic rheumatoid arthritis. Ann Rheum Dis 34:292–297
4. Resnick D (1976) Roentgen features of the rheumatoid mid- and hindfoot. J Can Assoc Radiol 27:99–107
5. Resnick D, Niwayama G (1981) Rheumatoid arthritis, diagnosis of bone and joint disorders. WB Saunders 906–1007
6. Spiegel TM, Spiegel JS (1982) Rheumatoid arthritis in the foot and ankle—diagnosis, pathology, and treatment. The relationship between foot and ankle deformity and disease duration in 50 patients. Foot Ankle 2:318–324
7. Vahvanen VA (1967) Rheumatoid arthritis in the pantalar joints. A follow-up study of triple arthrodesis on 292 adult feet. Acta Orthop Scand Suppl 107:9–143
8. Calabro JJ (1962) A critical evaluation of the diagnostic features of the feet in rheumatoid arthritis. Arthritis Rheum 5:19–29
9. Abdo RV, Iorio LJ (1994) Rheumatoid arthritis of the foot and ankle. J Am Acad Orthop Surg 12:326–332
10. Bouysset M, Tebib JG, Weil G et al (1987) Deformation of the adult rheumatoid rearfoot. A radiographic study. Clin Rheumatol 6:539–544
11. Cracchiolo A (1997) Rheumatoid arthritis. Hindfoot disease. Clin Orthop Relat Res 340:58–63
12. Arnett FC, Edworthy SM, Bloch DA et al (1988) The American Rheumatism Association 1987 revised criteria for the classification of rheumatoid arthritis. Arthritis Rheum 31:315–24
13. Bouyssett M, Bonvoisin B, Lejeune E et al (1987) Flattening of the rheumatoid foot in tarsal arthritis on X-ray. Scand J Rheumatol 16:127–133
14. Bouysset M, Bonvoisin B, Lepiller PH et al (1984) Empreinte plantaire encree et profil radiologique du pied dans la polyarthrite rhumatoide. Lyon Med 251:497
15. Djian A, Annonier CL, Denis A (1968) Radiopodometrie (Principles et resultants.). J Radiol Electrol Med Nucl 49: 769–772
16. Montagne J, Chevrot A, Galmiche JM (1980) In atlas de radiology du pied. Editor Masson Paris. 44–53
17. Gentili A, Masih S, Yao L et al (1996) Pictorial review: foot axes and angles. Br J Radiol 69:968–974
18. Shi K, Tomita T, Hayashida K et al (2000) Foot deformities in rheumatoid arthritis and relevance of disease severity. J Rheumatol 27:84–89
19. Bouyssett M, Tavernier T, Tebib J et al (1995) CT and MRI evaluation of tenosynovitis of the rheumatoid hindfoot. Clin Rheumatol 14:303–307
20. Michelson J, Easley M, Wigley FM et al (1995) Posterior tibial tendon dysfunction in rheumatoid arthritis. Foot Ankle Int 16:156–161

THE JOURNAL OF BIOLOGICAL CHEMISTRY VOL. 283, NO. 40, pp. 27154–27164, October 3, 2008

Smad7 Inhibits Chondrocyte Differentiation at Multiple Steps during Endochondral Bone Formation and Down-regulates p38 MAPK Pathways*•

Received for publication, February 13, 2008, and in revised form, July 17, 2008 Published, JBC Papers in Press, July 21, 2008, DOI 10.1074/jbc.M801175200

Takao Iwai[‡§], **Junko Murai**[‡§], **Hideki Yoshikawa**[§], **and Noriyuki Tsumaki**[‡1]

From the Departments of [‡]*Bone and Cartilage Biology and* [§]*Orthopaedic Surgery, Osaka University Graduate School of Medicine, 2-2 Yamadaoka, Suita, Osaka 565-0871, Japan*

Bone morphogenetic proteins (BMPs) play critical roles at various stages in endochondral bone formation. *In vitro* studies have demonstrated that Smad7 regulates transforming growth factor-β and BMP signals by inhibiting Smad pathways in chondrocytes. However, the *in vivo* roles of Smad7 during cartilage development are unknown. To investigate distinct effects of Smad7 at different stages during chondrocyte differentiation, we generated a series of conditional transgenic mice that overexpress Smad7 in chondrocytes at various steps of differentiation by using the Cre/loxP system. We generated *Col11a2-lacZ*^{floxed}*-Smad7* transgenic mice and mated them with three types of Cre transgenic mice to obtain *Smad7*^{Prx1}, *Smad7*^{11Enh}, and *Smad7*^{11Prom} conditional transgenic mice. *Smad7*^{Prx1} mice overexpressing Smad7 in condensing mesenchymal cells showed disturbed mesenchymal condensation associated with decreased Sox9 expression, leading to poor cartilage formation. *Smad7*^{11Enh} mice overexpressing Smad7 in round chondrocytes showed decreased chondrocyte proliferation rates. *Smad7*^{11Prom} mice overexpressing Smad7 in flat chondrocytes showed inhibited maturation of chondrocytes toward hypertrophy. Micromass culture of mesenchymal cells showed that BMP-induced cartilaginous nodule formation was down-regulated by overexpression of Smad7, but not Smad6. Overexpression of Smad7, but not Smad6, down-regulated the phosphorylation of p38 MAPKs. Our data provide *in vivo* evidence for distinct effects of Smad7 at different stages during chondrocyte differentiation and suggest that Smad7 in prechondrogenic cells inhibits chondrocyte differentiation possibly by down-regulating BMP-activated p38 MAPK pathways.

The transforming growth factor-β (TGF-β)[2] superfamily regulates cell growth and differentiation in a variety of tissues. This family includes three major subfamilies: TGFs-β, activins, and bone morphogenetic proteins (BMPs). Signaling by members of the TGF-β superfamily is transduced through type I and II serine/threonine kinase receptors (1). Upon ligand binding, type II receptors phosphorylate type I receptors. Next, type I receptors phosphorylate downstream targets. Receptor-regulated Smads (R-Smads) are phosphorylated by type I receptors (2). Smad1, Smad5, and Smad8 are R-Smads that transduce BMP signals, and Smad2 and Smad3 are R-Smads that transduce TGF-β and activin signals. Phosphorylated R-Smads form heteromers with Smad4, which is a common-partner Smad (referred to as Co-Smad), and translocate into the nucleus. There, they interact with transcription factors and activate gene transcription. Although the Smad pathway exists in most cell types and tissues, additional pathways are activated by BMP/TGF-β in certain cell types (3). BMP and TGF-β activate TAK1 (TGF-β-activated kinase 1), a member of the MAPK kinase kinase family. TAK1 is involved in the activation of several MAPKs, including JNK, p38, and ERK, which ultimately results in the activation of ATF2. TGF-β also activates Rho signaling pathways.

Inhibitory Smads including Smad6 and Smad7 inhibit phosphorylation of R-Smads by competing with R-Smads for binding to phosphorylated type I receptors (2). Smad6 inhibits BMP signaling, whereas Smad7 inhibits both TGF-β and BMP signaling. Smad6 has narrow specificity in its interaction with receptors (4). Smad6 and Smad7 inhibit BMP-activated p38 MAPK pathways in neuronal cells (5). Smad6 and Smad7 interact differently with TAK1 in PC12 cells. Smad6 and Smad7 are differentially expressed during development (6). Mice deficient in exon 1 of Smad7 have abnormal B-cell responses and are small (7). Data on skeletal tissues of these mice are not available. These mice have partial Smad7 function because N-terminally truncated forms of the Smad7 transcript may be produced (7).

During development, the limb skeleton is formed through endochondral bone formation, which consists of multiple steps of cellular differentiation (8, 9). Mesenchymal cells initially undergo condensation, which is followed by the differentiation of prechondrogenic cells within these condensations into round chondrocytes to form cartilage. Round chondrocytes in cartilage proliferate and produce cartilage extracellular matrix composed of collagen fibrils and proteoglycans. Proliferating chondrocytes in the central region of the cartilage then exit the cell cycle and differentiate into hypertrophic chondrocytes. The proliferating chondrocytes closest to the hypertrophic

* This work was supported in part by Scientific Research Grants 18390415 and 19659378 from the Ministry of Education, Culture, Sports, Science, and Technology of Japan and by Health and Labor Sciences of Japan research grants. The costs of publication of this article were defrayed in part by the payment of page charges. This article must therefore be hereby marked "*advertisement*" in accordance with 18 U.S.C. Section 1734 solely to indicate this fact.

• This article was selected as a Paper of the Week.

[1] To whom correspondence should be addressed. Fax: 81-6-6879-3559; E-mail: ntsumaki@dbcb.med.osaka-u.ac.jp.

[2] The abbreviations used are: TGF-β, transforming growth factor-β; BMP, bone morphogenetic protein; R-Smad, receptor-regulated Smad; MAPK, mitogen-activated protein kinase; JNK, c-Jun N-terminal kinase; ERK, extracellular signal-regulated kinase; dpc, day(s) postcoitus; rhBMP2, recombinant human BMP2; RT, reverse transcription; X-gal, 5-bromo-4-chloro-3-indolyl-β-D-galactopyranoside.

chondrocytes flatten out and form orderly columns of still proliferating flat chondrocytes. The zone of the hypertrophic chondrocytes is invaded by blood vessels along with osteoblasts, osteoclasts, and hematopoietic cells to form primary ossification centers. BMPs play critical roles at various stages in endochondral bone formation (10). Cartilage formation is severely disturbed in mice lacking BMP receptors (11) and in mice overexpressing *Noggin*, a BMP antagonist (12), in prechondrogenic cells; these results suggest that BMP signaling is necessary for cartilage formation.

Smad7 is expressed in growth plate cartilage (13) and osteoarthritic cartilage (14, 15). *In vitro* studies using cell culture systems or organ culture of mandibular explants have shown that Smad7 inhibits chondrocyte differentiation and/or proliferation induced by TGF-β (16, 17) or BMP (18, 19). These *in vitro* studies have demonstrated down-regulation of R-Smad activation by Smad7 in chondrocytes. On the other hand, recent mouse genetic studies have revealed mild abnormalities in cartilage in mice lacking Smad4 (20) and in mice overexpressing Smad6 (21) in chondrocytes, raising the possibilities that non-Smad pathways may also mediate BMP-induced cartilage formation. In addition, conditional inactivation of the TGF-β type II receptor gene (*Tgfbr2*) in prechondrogenic cells and chondrocytes results in mice without any long bone defects, leading to the conclusion that TGF-β signaling is not needed in the limb endochondral process (22). *In vivo* effects of Smad7 on cartilage development are unknown and thus are worth examining.

To examine the effects of Smad7 during cartilage development, we generated a series of conditional transgenic mice that overexpress Smad7 in chondrocytes at various steps of differentiation by using the Cre/loxP system. Smad7 overexpression in prechondrogenic cells disturbed mesenchymal condensation, leading to poor cartilage formation. Smad7 overexpression in round chondrocytes inhibited cell proliferation, and Smad7 overexpression in flat chondrocytes delayed hypertrophy. Micromass cultures of mesenchymal cells revealed that Smad7 inhibited cartilaginous nodule formation possibly by down-regulating p38 MAPK pathways activated by BMP.

EXPERIMENTAL PROCEDURES

Construction of the Transgene—The α2(XI) collagen gene (*Col11a2*)-based expression vector, p742*lacZ*Int, contains the *Col11a2* promoter (−742 to +380), an SV40 RNA splice site, the β-galactosidase reporter gene (*lacZ*), the SV40 polyadenylation signal, and 2.3 kb of the first intron sequence of *Col11a2* as an enhancer (23). To create a *Col11a2-lacZ^{floxed}-Smad7* transgene plasmid, a *loxP* sequence was inserted into the 5′-untranslated region of *lacZ* p742*lacZ*Int, and the NotI sites at both ends of the *lacZ* segment were mutated and abolished. Next, a sequence consisting of an SV40 RNA splice site, a *loxP* sequence, a NotI site, and the SV40 polyadenylation signal was inserted into the 3′-end of the SV40 polyadenylation signal of the plasmid. Finally, mouse Smad7 cDNA tagged with NotI sites at both ends was inserted into the NotI site. To create the *Col11a2prom-Cre-enh* plasmid, the *lacZ* sequence in p742*lacZ*Int was replaced with a NotI-tagged *Cre* sequence at the NotI sites. To create the *Col11a2prom-Cre* plasmid, the *lacZ* sequence in p742*lacZ* (23) was replaced with a NotI-tagged *Cre* sequence at NotI sites.

Generation and Preparation of Transgenic Mice—The plasmids *Col11a2-lacZ^{floxed}-Smad7*, *Col11a2prom-Cre-enh*, and *Col11a2prom-Cre* were digested with EcoRI and PstI to release the inserts. Transgenic mice were produced by microinjecting each of the inserts into the pronuclei of fertilized eggs from F_1 hybrid mice (C57BL/6 × DBA) as described previously (23). Transgenic embryos were identified by PCR assays of genomic DNA extracted from the placenta or skin. For *Col11a2-lacZ^{floxed}-Smad7* transgenic mice, primers derived from mouse Smad7 cDNA (5′-GGA TGG CGT GTG GGT TTA-3′) and from the SV40 poly(A) signal region (5′-GGT TTG TCC AAA CTC ATC AAT-3′) were used to amplify a 346-bp product. For Cre transgenic mice, primers derived from *Cre* (5′-CAA TTT ACT GAC CGT ACA CCA A-3′ and 5′-TCT TCA GGT TCT GCG GG-3′) were used to amplify a 187-bp product. *Prx1-Cre* transgenic mice were a kind gift from Dr. Malcolm Logan (24). *Col11a2-lacZ^{floxed}-Smad7* transgenic mice were mated with *Prx1-Cre*, *Col11a2prom-Cre-enh*, or *Col11a2prom-Cre* transgenic mice to obtain various Smad7 conditional transgenic mice. Conventional *Col11a2-Smad6* transgenic mice were described previously (21).

Staining of the Skeleton—Embryos were dissected, fixed in 100% ethanol overnight, and then stained with Alcian blue followed by alizarin red S solution according to standard protocols (25).

Histological Analysis—Embryos were dissected with a stereomicroscope, fixed in 4% paraformaldehyde, processed, and embedded in paraffin. Serial sections were stained with hematoxylin and eosin or with safranin O/fast green/iron hematoxylin. Immunohistochemistry was performed with a rabbit polyclonal antibody against Smad7 (1:100 dilution; Santa Cruz Biotechnology, Inc.). Immune complexes were detected using streptavidin-peroxidase staining and Histofine SAB-PO kits (Nichirei, Tokyo, Japan). RNA *in situ* hybridization was performed using ^{35}S-labeled antisense riboprobes as described previously (45). To detect proliferating cells in tissue sections, digoxigenin-11-UTP-labeled *Hist2* (histone cluster 2) RNA probes were prepared (26).

Micromass Culture of Mesenchymal Cells—Micromass culture was performed according to previously described methods (27). The distal quarters of limb buds from 12.0-day postcoitus (dpc) wild-type and transgenic mouse embryos were dissected and digested with 0.1% collagenase (Sigma) and 0.1% trypsin (Sigma) for 45 min in 5% CO_2 at 37 °C. The dissociated cells were filtered through nylon mesh (40-μm pore size; Tokyo Screen, Tokyo) to generate a single cell suspension and were then adjusted to 2×10^7 cells/ml in Dulbecco's modified Eagle's medium (Sigma) supplemented with 10% fetal bovine serum. Cell suspensions (20-ml drops) were placed in the center of each well of 12-well plates. After the cells were allowed to attach for 90 min in 10% CO_2 at 37 °C, they were overlaid with 2 ml of Dulbecco's modified Eagle's medium containing 10% fetal bovine serum. The medium was replaced by fresh medium every other day.

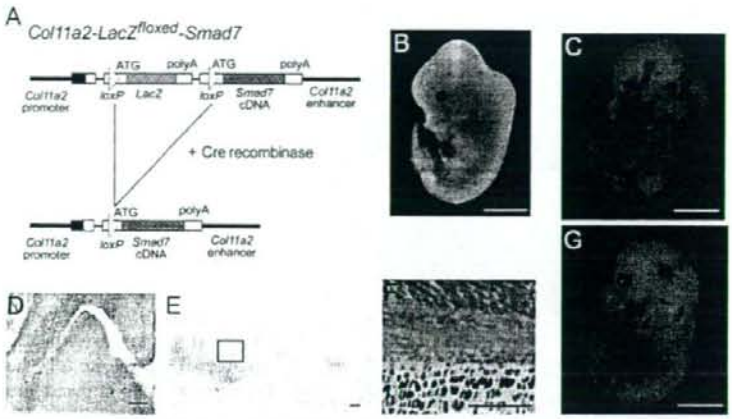

FIGURE 1. **Generation of *Col11a2-lacZ^floxed-Smad7* transgenic mice.** *A*, the structure of the *Col11a2-lacZ^floxed-Smad7* transgene is shown. In the presence of Cre recombinase, the *lacZ* sequence would be excised, and Smad7 would be expressed instead of LacZ under the control of the *Col11a2* promoter/enhancer sequences. *B–G*, two *Col11a2-lacZ^floxed-Smad7* transgenic mouse lines were established. Both lines showed similar cartilage-specific patterns of X-gal staining and developed normally. One line (*B–F*) showed stronger X-gal staining than the other line (*G*). *B*, at 12.5 dpc, mesenchymal condensation in limbs was strongly stained. *C*, at 14.5 dpc, primordial cartilage in limbs and ribs showed X-gal staining. *D*, a histological section showed X-gal-stained mesenchymal condensation in the forelimb at 12.5 dpc. *E*, shown is a histological section of the femur at 14.5 dpc. *F*, a higher magnification of the *boxed* region in *E* is shown. *G*, the other transgenic line at 14.5 dpc showed weak X-gal staining compared with the first line (*C*). *Scale bars* = 2.5 mm (*B* and *C*), 100 μm (*D* and *E*), 50 μm (*F*), and 2.5 mm (*G*).

To induce cartilaginous nodule formation, medium containing 50 or 100 ng/ml recombinant human BMP2 (rhBMP2) (Astellas Pharma, Tokyo) in 10% fetal bovine serum was used unless specifically described otherwise. For infection with adenoviral vectors for Smad6 and Smad7 (18), cells were infected 1 day after plating. For Alcian blue staining, micromass cultures 4 days after plating were fixed with 4% paraformaldehyde for 10 min and stained overnight with 1% Alcian blue in 3% acetic acid at 37 °C. The cultures were then digitally photographed with a Nikon SMZ-U microscope. The size and number of nodules were measured using WinROOF software (Mitani Shoji, Fukui, Japan). For Western blot analysis, adenovirus-infected cells were starved for 16 h before replacement with Dulbecco's modified Eagle's medium in the presence or absence of rhBMP2. Cells were lysed 1 h after treatment with rhBMP2. For activation of MAPK pathways, 2 ng/ml anisomycin (Sigma) was added to the culture medium and used as a positive control.

Total RNA extracted from micromass culture in the presence of 100 ng/ml rhBMP2 was digested with DNase to eliminate any contaminating genomic DNA before real-time quantitative reverse transcription (RT)-PCR. Real-time RT-PCR was performed as described previously (21). The primer pair for *Id1* was as follows: up, 5′-GCA TCT TGT GTC GCT GAG-3′; and down, 5′-TGG CTG CGG TAG TGT CTT-3′. The product size was 122 bp.

ATDC5 Cell Culture—ATDC5 cells were a kind gift from Dr. Y. Hiraki. The cells were maintained at 20–80% confluency as described previously (28). After infection of ATDC5 cells with adenoviral vectors for LacZ, Smad6, Smad7, and constitutively active MKK3, the cells were washed and then starved for 16 h. The medium was replaced with Dulbecco's modified Eagle's medium in the presence or absence of rhBMP2. One hour after treatment with rhBMP2, the cells were lysed and subjected to Western blotting. For activation of MAPK pathways, 2 ng/ml anisomycin was added to the culture medium and used as a positive control.

Western Blotting—Cells were cultured, lysed, subjected to SDS-PAGE, electroblotted, and immunostained. The antibodies used were anti-Smad7 antibody (1:200 dilution; Santa Cruz Biotechnology, Inc.); anti-Smad6 antibody (1:200 dilution; Zymed Laboratories Inc.), anti-Smad1 antibody (1:1000 dilution; Calbiochem); anti-phospho-Smad1/5/8 antibody (1:1000 dilution), anti-phospho-ATF2 antibody (1:1000 dilution), anti-ATF2 antibody (1:1000 dilution), anti-phospho-p38 MAPK antibody (1:1000 dilution), anti-p38 MAPK antibody (1:1000 dilution), anti-phospho-Smad2 antibody (1:1000 dilution), and anti-Smad2/3 antibody (1:1000 dilution) (Cell Signaling Technology). Proteins in the blots were visualized using an ECL Plus kit (Amersham Biosciences).

RESULTS

Generation of Floxed lacZ-Smad7 Transgenic Mice—Because Smad7 inhibits various signaling pathways, we anticipated that its overexpression in chondrocytes might cause severe cartilage abnormalities in transgenic mice. To avoid lethality, we employed a conditional transgenic mouse system to express the *Smad7* transgene. We first established floxed *lacZ-Smad7* transgenic mouse lines bearing the *Col11a2-lacZ^floxed-Smad7* transgene (Fig. 1*A*). *Col11a2* promoter/enhancer sequences direct expression to condensed mesenchymal cells and chondrocytes (23). We expected that the mice bearing this construct would express *lacZ* but not Smad7 due to the poly(A) signal sequence that immediately follows the *lacZ* sequence. In the presence of Cre recombinase, the *lacZ* sequence would be deleted, and Smad7 would be expressed instead of *lacZ* under the control of the *Col11a2* promoter/enhancer sequences. We obtained and analyzed two independent lines of *Col11a2-lacZ^floxed-Smad7* transgenic mice. Staining of transgenic embryos from one line with X-gal showed that *lacZ* was expressed in condensed mesenchyme at 12.5 dpc (Fig. 1*B*) and in primordial cartilage in limbs and ribs at 14.5 dpc (Fig. 1*C*). Histological analysis confirmed *lacZ* activities specifically in mesenchymal condensation at 12.5 dpc (Fig. 1*D*) and in chondrocytes at 14.5 dpc (Fig. 1*E*). *lacZ* activities were not recognized in cells in the perichondrium (Fig. 1*F*). Transgenic embryos from the other line showed a similar but weaker (Fig. 1*G*) pattern of *lacZ* activities than the first line (Fig. 1*C*) at 14.5 dpc. Both lines of mice developed normally.

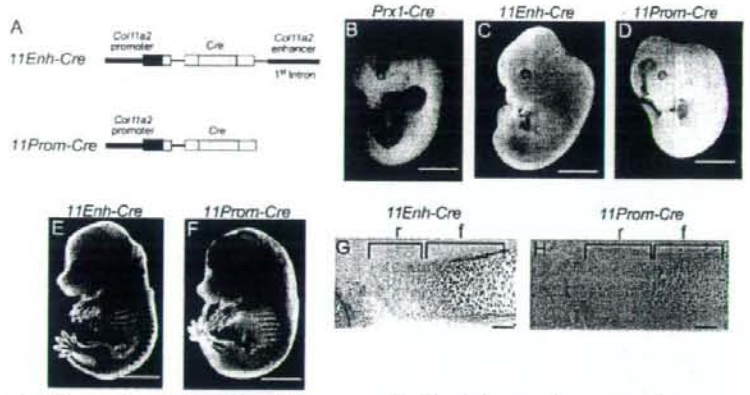

FIGURE 2. **Preparation of three types of Cre transgenic mice.** *A*, shown is the structure of *11Enh-Cre* and *11Prom-Cre* transgenes. *B–H*, three types of Cre transgenic mice were mated with *CAG-CAT*^{floxed}*-lacZ* tester mice, and the progeny were examined for LacZ expression by X-gal staining. *B–D*, the patterns of Cre-catalyzed recombination at 12.5 dpc are shown. *Prx1-Cre* transgenic mice had recombination throughout their limb buds (24) (*B*). *11Enh-Cre* directed very weak recombination only in mesenchymal condensation in forelimbs (*C*). *11Prom-Cre* directed no recombination in the limbs or trunk (*D*). *E* and *F*, shown are the patterns of Cre-catalyzed recombination at 14.5 dpc. *11Enh-Cre* directed recombination in the entire parts of each primordial cartilage (*E*). *11Prom-Cre* directed recombination in limited parts of each primordial cartilage (*F*). *G* and *H*, histological sections of the forelimb at 14.5 dpc are shown. *11Enh-Cre* directed recombination in all round and flat proliferative chondrocytes (*G*). *11Prom-Cre* directed recombination in flat proliferative chondrocytes, but not in round proliferative chondrocytes (*H*). *r*, zone of round proliferative chondrocytes; *f*, zone of flat proliferative chondrocytes. *Scale bars* = 2.5 mm (*B–F*) and 100 μm (*G* and *H*).

Generation of Cre Transgenic Mice—Next, we prepared three types of Cre transgenic mice. First, *Prx1-Cre* transgenic mice were obtained from Dr. Malcolm Logan (24). Second, we linked the *Cre* sequence to the *Col11a2* promoter plus intron enhancer to prepare the transgene construct *11Enh-Cre* (Fig. 2*A*). Third, we prepared *Cre* linked to the *Col11a2* promoter without an intron enhancer to prepare the transgene construct *11Prom-Cre* (Fig. 2*A*). We injected *11Enh-Cre* and *11Prom-Cre* into fertilized ova and established transgenic lines.

We examined the expression patterns of Cre by mating *CAG-CAT*^{floxed}*-lacZ* reporter transgenic mice (29) with these Cre transgenic mice. As reported previously (24), *Prx1-Cre* mice showed Cre recombinase activity throughout the early limb bud mesenchyme at 12.5 dpc. (Fig. 2*B*). *11Enh-Cre* transgenic mice started to show very weak Cre activities in mesenchymal condensation in forelimb buds at 12.5 dpc (Fig. 2*C*). *11Prom-Cre* transgenic mice showed no *lacZ* activities in limb buds at 12.5 dpc (Fig. 2*D*). Aberrant Cre activities were recognized in forebrains. At 14.5 dpc, *11Enh-Cre* transgenic mice showed Cre-mediated recombination in all primordial cartilage of limbs and ribs (Fig. 2*E*). In contrast, *11Prom-Cre* transgenic mice showed recombination in a limited part of each primordial cartilage (Fig. 2*F*). X-gal staining was absent in the epiphyseal part of each primordial cartilage. Histological analysis of the distal ulnas of *11Enh-Cre* transgenic mice at 14.5 dpc showed recombinase activities in all chondrocytes, including round proliferative chondrocytes, flat proliferative chondrocytes, prehypertrophic chondrocytes, hypertrophic chondrocytes, and perichondrial cells (Fig. 2*G*). Histological analysis of the distal ulnas of *11Prom-Cre* transgenic mice at 14.5 dpc showed recombinase activities in flat chondrocytes, prehypertrophic chondrocytes, and hypertrophic chondrocytes, but not in round chondrocytes located at the ends of each primordial cartilage (Fig. 2*H*). These results suggest that *11Enh-Cre* induces recombination from the step of round proliferative chondrocytes and that *11Prom-Cre* induces recombination from the step of flat proliferative chondrocytes. The recombination pattern of our *11Enh-Cre* transgenic mice was consistent with that of previously reported Cre transgenic mice containing identical promoter/enhancer sequences (30). None of the Cre transgenic mice showed detectable abnormalities.

Skeletal Abnormalities in Smad7 Conditional Transgenic Mice—We mated *Col11a2-lacZ*^{floxed}*-Smad7* transgenic mice with *Prx1-Cre*, *11Enh-Cre*, and *11Prom*-Cre transgenic mice, respectively, and generated double transgenic pups as follows: pups bearing *Col11a2-lacZ*^{floxed}*-Smad7* and *Prx1-Cre* transgenes (*Smad7*^{Prx1}), those bearing *Col11a2-lacZ*^{floxed}*-Smad7* and *11Enh-Cre* transgenes (*Smad7*^{11Enh}), and those bearing *Col11a2-lacZ*^{floxed}*-Smad7* and *11Prom-Cre* transgenes (*Smad7*^{11Prom}). We examined the skeletons of Smad7 conditional transgenic mice. Staining with Alcian blue and alizarin red S revealed that the *Smad7*^{Prx1} double transgenic mice had very hypoplastic limb skeletons (Fig. 3*B*) compared with *Col11a2-lacZ*^{floxed}*-Smad7* control mice (Fig. 3*A*) at 16.5 dpc. The *Smad7*^{Prx1} axial skeleton was relatively preserved because the *Prx1-Cre* transgene directs Cre expression mainly in limbs. Hind limb skeletons were less affected than forelimb skeletons. *Smad7*^{11Enh} mice had moderately hypoplastic skeletons (Fig. 3*C*) compared with *Col11a2-lacZ*^{floxed}*-Smad7* control mice (Fig. 3*A*). Mineralization indicated by alizarin red staining was reduced in *Smad7*^{11Enh} mice. The cartilaginous components of *Smad7*^{11Prom} mice were slightly small (Fig. 3*D*) compared with those of *Col11a2-lacZ*^{floxed}*-Smad7* control mice (Fig. 3*A*). Mineralization was reduced slightly in *Smad7*^{11Prom} mice. We also mated the other line of *Col11a2-lacZ*^{floxed}*-Smad7* mice with *Prx1-Cre* mice, and the resultant *Smad7*^{Prx1} transgenic pups showed similar but milder abnormalities in limb skeleton (Fig. 3*E*) than the *Smad7*^{Prx1} mice from the first line of *Col11a2-lacZ*^{floxed}*-Smad7* mice (Fig. 3*B*). Overall, the skeletal lengths in each type of double transgenic pups varied with regard to cartilage size and mineralization depending on the types of Cre transgenic mice used for mating (Fig. 3*F*).

Cre-mediated Recombination in Each Type of Conditional Transgenic Mice—The scheme in Fig. 4*A* shows the expected recombination events in this experiment. In *Smad7*^{Prx1} mice, recombination occurs in mesenchymal cells in limb buds before the onset of mesenchymal condensation when *Col11a2* promoter/enhancer sequences start to direct expression. Thus, the

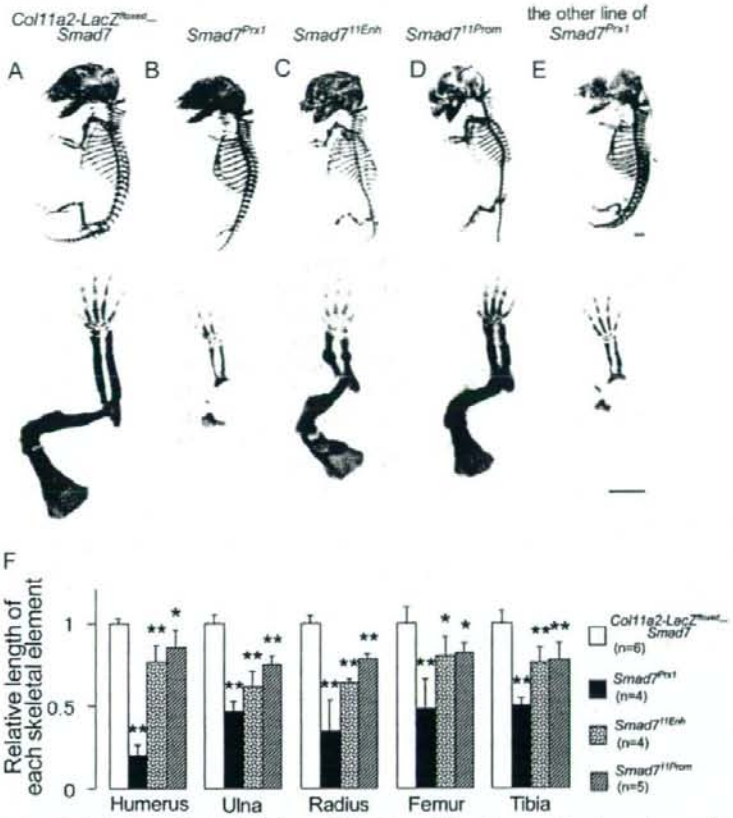

FIGURE 3. **Whole body and forelimb skeleton of Smad7 conditional transgenic mice and conventional Smad6 transgenic mice at 16. 5 dpc.** *A*, *Col11a2-lacZ*^{floxed}*-Smad7* mice (control). *B*, *Col11a2-lacZ*^{floxed}*-Smad7; Prx1-Cre* mice (*Smad7*^{Prx1}). *C*, *Col11a2-lacZ*^{floxed}*-Smad7;11Enh-Cre* mice (*Smad7*^{11Enh}). *D*, *Col11a2-lacZ*^{floxed}*-Smad7;11Prom-Cre* mice (*Smad7*^{11Prom}). When we mated the other line of *Col11a2-lacZ*^{floxed}*-Smad7* mice that showed weaker *lacZ* activities (Fig. 1*G*) with *Prx1-Cre* transgenic mice, the resultant double transgenic pup (*E*) showed similar but milder skeletal abnormalities than that (*B*) from the *Col11a2-lacZ*^{floxed}*-Smad7* mouse line, which showed stronger *lacZ* activities (Fig. 1*C*). *F*, relative length of 16.5-dpc skeletal elements of conditional transgenic mice. *Error bars* indicate means ± S.D. *, $p < 0.05$; and **, $p < 0.01$ between control and transgenic skeletal elements as determined by Student's *t* test. *Scale bar* = 1 mm.

expression of the *Smad7* transgene in *Smad7*^{Prx1} mouse limbs may be controlled by *Col11a2* promoter/enhancer sequences in the *Col11a2-lacZ*^{floxed}*-Smad7* transgene, and the *Smad7* transgene may be gradually expressed from the step of condensed mesenchyme. The expression pattern of the *Smad7* transgene in *Smad7*^{Prx1} conditional transgenic mouse limbs is considered to be similar to the expression pattern of the transgene expression in conventional transgenic mice bearing the *Col11a2* promoter/enhancer. In *Smad7*^{11Enh} mice, recombination occurs at the step of round proliferative chondrocytes when the amount of Cre protein may be increased enough to catalyze recombination. In *Smad7*^{11Prom} mice, recombination occurs at the step of flat proliferative chondrocytes.

We examined Cre-catalyzed recombination by monitoring the disappearance of *lacZ* activities. *Col11a2-lacZ*^{floxed}*-Smad7* mice showed LacZ expression in condensed mesenchyme at 12.5 dpc (Fig. 4*B*). *Smad7*^{Prx1} double transgenic mice did not exhibit LacZ expression (Fig. 4*C*), indicating that *Prx1-Cre* transgene products induced recombination of the *Col11a2-lacZ*^{floxed}*-Smad7* transgene in limb buds. Both *Smad7*^{11Enh} mice and *Smad7*^{11Prom} mice showed LacZ expression in condensed mesenchyme (Fig. 4, *D* and *E*), as did *Col11a2-lacZ*^{floxed}*-Smad7* control mice (Fig. 4*B*), indicating that recombination did not occur at this stage.

At 14.5 dpc, *Col11a2-lacZ*^{floxed}*-Smad7* control mice showed LacZ expression in all primordial cartilage (Fig. 4*F*). *Smad7*^{Prx1} mice showed LacZ expression in primordial cartilage in the ribs and spine, but not in the limbs (Fig. 4*G*). LacZ expression in *Smad7*^{11Enh} mice disappeared in primordial cartilage in trunk and proximal segments in the limbs. LacZ expression remained in paws, which developed later than proximal segments in the limbs (Fig. 4*H*). *Smad7*^{11Prom} mice showed LacZ expression in most of the primordial cartilage at this stage except for weak LacZ expression in the humerus and femur, which developed earlier than the distal segments (Fig. 4*I*).

Histological Analysis of Various Smad7 Conditional Transgenic Mice—To investigate the function of Smad7 at various steps during endochondral bone formation, we performed histological analysis of skeletons of Smad7 conditional transgenic mice bearing various *Cre* transgenes. At 16.5 dpc, wild-type mice formed ossification centers in the humerus (Fig. 5*A*). *Smad7*^{Prx1} mice showed very small cartilage. The *Smad7*^{11Enh} transgenic cartilage of the humerus contained proliferative and hypertrophic chondrocytes, but not ossification centers. The humeri of *Smad7*^{11Prom} mice had an almost normal sized proliferative cartilage and exhibited incomplete formation of ossification centers.

At 14.5 dpc, proliferative chondrocytes started hypertrophy at the center of the humeri of wild-type mice (Fig. 5*B*). The *Smad7*^{11Prom} transgenic cartilage from the humerus contained proliferative (but not hypertrophic) chondrocytes. These results suggest that Smad7 expressed in flat proliferative chondrocytes delays chondrocyte hypertrophy.

Proliferation of Proliferative Chondrocytes Is Inhibited by Smad7 Overexpression—We examined the effect of Smad7 overexpression on the proliferation of proliferative chondrocytes by *in situ* hybridization using *Hist2* cRNA probes on histological sections of distal femur at 16.5 dpc and performed statistical analysis (Fig. 5, *C* and *D*). *In situ* hybridization for

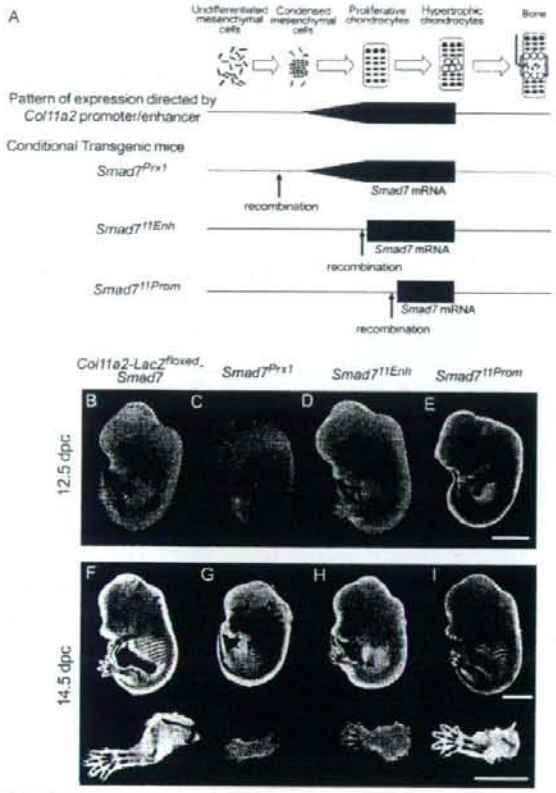

FIGURE 4. **Cre-catalyzed recombination in Smad7 conditional transgenic mice.** *A*, expected recombination events during the endochondral bone formation process in Smad7 transgenic mice. *Top row*, pattern of expression directed by the *Col11a2* promoter/enhancer. *Second* through *fourth rows*, expected *Smad7* transgene expression patterns in each Smad7 conditional transgenic mouse. *B–E*, Cre-catalyzed recombination monitored by the disappearance of *lacZ* activities in Smad7 conditional transgenic mice at 12.5 dpc. LacZ expression was abolished in mesenchymal condensation in $Smad7^{Prx1}$ mice (*C*). LacZ expression in mesenchymal condensation was not obviously affected in $Smad7^{11Enh}$ mice (*D*) and $Smad7^{11Prom}$ mice (*E*). *F–I*, Cre-catalyzed recombination at 14.5 dpc. *Prx1-Cre* completely abolished LacZ expression in limb cartilage, but not in trunk cartilage (*G*). *11Enh-Cre* eliminated *lacZ* activities in all primordial cartilage except the distal part of limbs (*H*). *11Prom-Cre* decreased *lacZ* activity in the humerus (*I*). *Scale bars* = 2.5 mm.

histone mRNA is as an appropriate technique for assessment of cell proliferation as bromodeoxyuridine immunohistochemistry (26). Compared with the control mice, $Smad7^{11Enh}$ double transgenic mice had a reduced number of *Hist2*-positive cells. In contrast, $Smad7^{11Prom}$ mice had a normal number of *Hist2*-expressing cells.

We analyzed the transgene expression in distal femur by *in situ* hybridization (Fig. 5*E*). In wild-type mice, the expression levels of Smad7 and Smad6 were relatively low in cartilage compared with those in the surrounding tissues. $Smad7^{11Enh}$ mice showed increased *Smad7* expression in both epiphyseal and metaphyseal chondrocytes, suggesting that Cre-mediated deletion of the *lacZ* sequence had occurred and that the *Smad7* transgene was transcribed in round and flat chondrocytes. $Smad7^{11Prom}$ mice showed increased Smad7 expression in the metaphyseal chondrocytes and *lacZ* expression in the epiphyseal chondrocytes, suggesting that Cre-mediated recombination had occurred and that the *Smad7* transgene was transcribed mainly in flat chondrocytes. Immunohistochemical analysis showed that anti-Smad7 immunoreactivity was increased in the femoral chondrocytes of $Smad7^{11Enh}$ double transgenic mice compared with those of wild-type mice, suggesting that *Smad7* transgene mRNA was translated (Fig. 5*F*).

Mesenchymal Condensation Is Inhibited and Sox9 Expression Is Decreased in $Smad7^{Prx1}$ Mice—We examined the mechanism responsible for hypoplastic cartilage in the limbs of $Smad7^{Prx1}$ transgenic mice. The loss of LacZ expression in limbs (shown in Fig. 4*C*) suggested condensed mesenchyme-specific expression of the *Smad7* transgene. *In situ* hybridization analysis of axial sections of 12.5-dpc wild-type limb buds showed that *Sox9* and *Col11a2* were expressed in condensing mesenchyme that was recognized in sections stained with safranin O (Fig. 6*A*). In $Smad7^{Prx1}$ mice, mesenchymal condensation was not apparent; *Sox9* expression was weak; and *Col11a2* expression was not detected at this stage. *In situ* hybridization analysis of mice at 16.5 dpc showed that the expression levels of Smad6 and Smad7 mRNAs in chondrocytes relatively low compared with the levels in the surrounding tissues in the wild-type mice. The relative expression levels of Smad7 in femoral chondrocytes were similar to those of Smad7 in surrounding tissues in $Smad7^{Prx1}$ mice (Fig. 6*B*). These results suggest that the *Smad7* transgene was transcribed mainly in chondrocytes.

Smad7 (but Not Smad6) Overexpression Inhibits Cartilaginous Nodule Formation Induced by BMP and Inhibits BMP-activated MAPK Pathways—Mouse genetic experiments have shown that BMP signal inactivation dramatically inhibits cartilage formation (11), but TGF-β signal inactivation does not affect cartilage formation in the limbs (22). To further examine how Smad7 overexpression inhibited cartilage formation, we analyzed BMP signals during cartilaginous nodule formation using micromass cultures of limb bud mesenchymal cells prepared from the first line of $Smad7^{Prx1}$ mice and the other line of $Smad7^{Prx1}$ mice. The other line of $Smad7^{Prx1}$ mice (Fig. 3*E*) showed less severe skeletal abnormalities than the first line of $Smad7^{Prx1}$ mice (Fig. 3*B*). We also prepared mesenchymal cells from *Col11a2-Smad6* transgenic mice, which express Smad6 in condensed mesenchymal cells and chondrocytes (21). The addition of rhBMP2 to the medium stimulated the formation of cartilaginous nodules, which were visualized by Alcian blue staining (Fig. 7*A*, *top row*). The cartilaginous nodule formation induced by rhBMP2 was decreased in mesenchymal cells prepared from the first line of $Smad7^{Prx1}$ mice (Fig. 7*A*, *second row*) and in mesenchymal cells prepared from the other line of $Smad7^{Prx1}$ mice (*third row*), but not in mesenchymal cells from *Col11a2-Smad6* transgenic mice (*fourth row*). The mean number of cartilaginous nodules was more in the mesenchymal cell cultures of the other line of $Smad7^{Prx1}$ mice (Fig. 7*A*, *third row*) than that in the mesenchymal cell cultures of the first line of $Smad7^{Prx1}$ mice (*second row*).

We next examined marker gene expression in micromass cultures of transgenic mesenchymal cells in the presence of rhBMP2 by real-time RT-PCR (Fig. 7*B*). The relative expression levels of *Smad7* were increased in mesenchymal cells from the

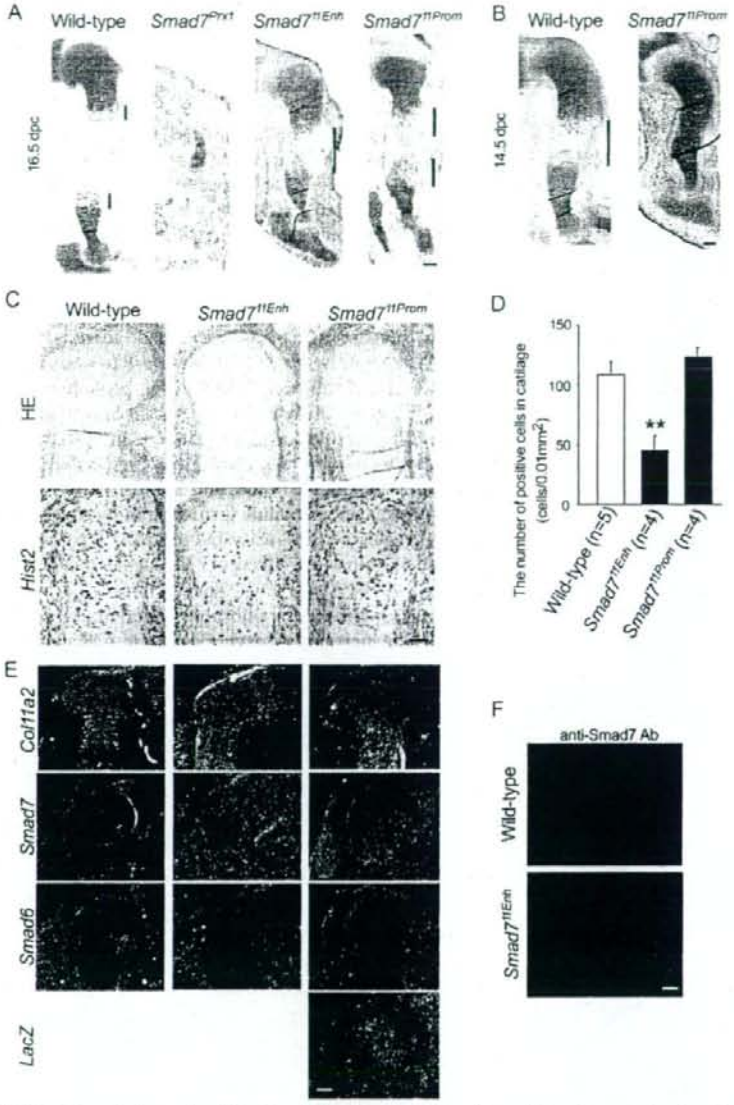

FIGURE 5. **Differentiation and proliferation of chondrocytes in Smad7 conditional transgenic mice.** *A*, histology of the humeri of *Smad7*^{Prx1}, *Smad7*^{11Enh}, and *Smad7*^{11Prom} mice at 16.5 dpc. The cartilage size was very small in *Smad7*^{Prx1} mice. *B*, histology of the humeri of *Smad7*^{11Prom} mice at 14.5 dpc. Chondrocyte hypertrophy was delayed. *C*, *in situ* hybridization with *Hist2* antisense cRNA probes in the 16.5-dpc distal femurs of *Smad7*^{11Enh} and *Smad7*^{11Prom} mice. The number of chondrocytes expressing *Hist2* was decreased in *Smad7*^{11Enh} femur. *HE*, hematoxylin and eosin. *D*, the mean number of chondrocytes expressing *Hist2* mRNAs per area in the distal femurs of *Smad7*^{11Enh} and *Smad7*^{11Prom} mice. *Error bars* indicate means ± S.D. **, $p < 0.01$ between wild-type and transgenic mice as determined by Student's *t* test. *E*, *in situ* hybridization analysis of 16.5-dpc distal femurs of *Smad7*^{11Enh} and *Smad7*^{11Prom} mice. *Col11a2*, *Smad6*, *Smad7*, and *lacZ* antisense cRNA probes were used. Distal femoral cartilage was demarcated. *r*, epiphyseal zone of round proliferative chondrocytes; *f*, metaphyseal zone of flat proliferative chondrocytes. *F*, immunohistochemistry of 16.5-dpc proximal humeri of *Smad7*^{11Enh} mice with anti-Smad7 antibody (*Ab*). *Scale bars* = 100 μm (*A–C* and *E*) and 50 μm (*F*).

first line of *Smad7*^{Prx1} mice, indicating transgene expression. The expression levels of *Smad6* were increased in mesenchymal cells from *Smad7*^{Prx1} mice, probably because the culture was composed mainly of non-cartilaginous cells. Non-chondrocytic cells expressed endogenous Smad6 at higher levels compared with chondrocytes (Fig. 6*B*). The relative expression levels of *Col2a1*, *Col11a2*, and *Sox9* were decreased, and the expression level of *Aldh1a2*, which is the target gene of BMP signals and down-regulates *Sox9* gene expression (31), was increased. In contrast, the relative expression levels of the maker genes were not significantly changed in mesenchymal cells from *Col11a2-Smad6* mice. The relative expression levels of *Smad6* were elevated in *Col11a2-Smad6* mice. These results revealed different effects on cartilaginous nodule formation and marker gene expression between Smad7 and Smad6 overexpression, although we could not deny the possibility that the expression level of the *Smad6* transgene was not high enough compared with that of the *Smad7* transgene.

Because Smad6 overexpression did not disturb cartilaginous nodule formation or marker gene expression, we speculated that non-Smad pathways might mediate BMP-induced nodule formation. It has been reported that BMPs activate MAPK pathways (3). MAPKs control chondrogenesis (32). JNK phosphorylation is not affected during chondrogenesis, suggesting that JNKs play minor roles (33). During chondrogenesis of chick mesenchymal cells, p38 phosphorylation is increased, and ERK phosphorylation is decreased. The inhibitor of p38 MAPK pathways blocks chondrogenesis, whereas the inhibitor of MEK/ERK activity enhances chondrogenesis (34). This line of findings suggests that p38 MAPK pathways may be involved in BMP-induced nodule formation.

Next, we examined whether our results from the transgenic overexpression experiments were consistent with results from the adenoviral overexpression experiments. Consistently, cartilaginous nodule formation in wild-type mouse mesenchymal cells was inhibited by Smad7 adenoviral infection (Fig. 7*C*, *second row*), but not by Smad6 adenoviral infection (*third row*). Real-time RT-PCR analysis showed that the relative mRNA expression levels for

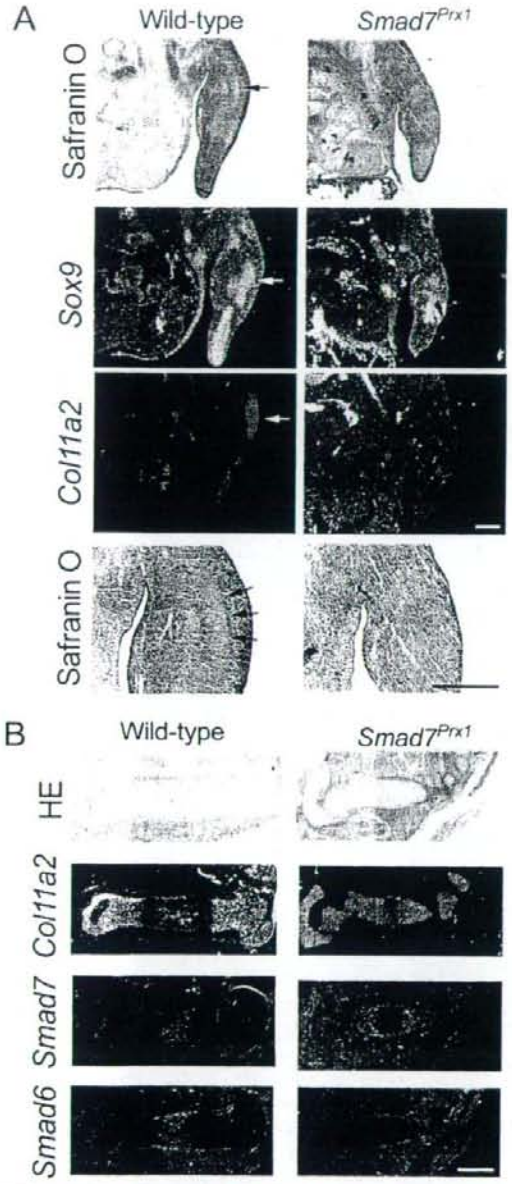

FIGURE 6. **Cartilage formation is inhibited by Smad7 overexpression.** *A*, semiserial axial sections at forelimb levels of *Smad7*^{Prx1} mouse embryos at 12.5 dpc were used for safranin O/fast green/iron hematoxylin staining (*top row*) and *in situ* hybridization analysis with *Sox9* (*second row*) and *Col11a2* (*third row*) antisense cRNA probes. *Sox9* expression was weak in *Smad7*^{Prx1} mice. Magnification of limbs showed that mesenchymal condensation was not apparent in *Smad7*^{Prx1} mice (*fourth row*). *Arrows* indicate mesenchymal condensation. *B*, semiserial sagittal sections of femurs in wild-type and *Smad7*^{Prx1} mice at 16.5 dpc were used for hematoxylin and eosin (*HE*) staining and *in situ* hybridization analysis with *Col11a2*, *Smad7*, and *Smad6* antisense cRNA probes. The expression levels of Smad7 mRNAs in chondrocytes were relatively low compared with the levels in the surrounding tissues in wild-type mice. The relative expression levels of Smad7 in femoral chondrocytes were similar to those of Smad7 in surrounding tissues in *Smad7*^{Prx1} mice. *Scale bars* = 50 μm (*A*) and 200 μm (*B*).

Smad7 and *Smad6* were elevated in micromass cultures infected with Smad7 and Smad6 adenoviral vectors, respectively (Fig. 7*D*). Both Smad6 and Smad7 adenoviral infection decreased the expression levels of *Id1*, the target gene of Smad1/5/8 (35, 36), suggesting that Smad1/5/8 pathways were affected. We used immunoblot analysis to examine the effects of BMP signals on the phosphorylation of signaling molecules in micromass cultures of wild-type mouse mesenchymal cells (Fig. 7*E*). The addition of rhBMP2 induced the phosphorylation of Smad1/5/8 but only slightly induced the phosphorylation of Smad2. The addition of rhBMP2 also induced the phosphorylation of p38 and ATF2, a downstream target molecule of the MAPK pathways, like anisomycin, a positive control for MAPK pathways. Infection with Smad7 and Smad6 adenoviral vectors inhibited the phosphorylation of Smad1/5/8 to similar extents. Smad7 adenoviral infection inhibited the phosphorylation of p38 and ATF2 to a greater extent than did Smad6 adenoviral infection. These results indicate the following. 1) Cartilaginous nodule formation induced by rhBMP2 was associated with activation of p38 MAPK pathways, and 2) Smad7 overexpression inhibited cartilaginous nodule formation induced by rhBMP2 and down-regulated BMP-activated p38 MAPK pathways.

We also examined the effects of BMP signals using an undifferentiated ATDC5 cell line. The addition of rhBMP2 to ATDC5 cells increased the phosphorylation of p38 and ATF2 (Fig. 8*A*). The increased phosphorylation of p38 and ATF2 in the presence of rhBMP2 was decreased by Smad7 adenoviral infection to a greater extent compared with Smad6 adenoviral infection. Infection with an adenoviral construct of a constitutively active form of MKK3 (a gift from Dr. Riko Nishimura), a MAPK kinase that activates p38 (37), increased the phosphorylation of p38 and ATF2 in ATDC5 cells (Fig. 8*B*). Infection with both the constitutively active form of MKK3 and the Smad7 adenoviral construct showed increased phosphorylation of p38 and ATF2, suggesting that Smad7 affects MAPK pathways upstream of MKK3 in ATDC5 cells.

DISCUSSION

Smad7 Overexpression Affects Cartilage Development at Multiple Steps—To examine the effects of Smad7 on cartilage at various stages of chondrocyte differentiation *in vivo*, we generated mice that conditionally overexpress Smad7 in chondrocytes. To avoid potential lethality, we employed a conditional transgenic mouse system. Conditional transgenic mouse systems that use Cre/loxP in other tissues have been developed previously (38, 39). We established *Col11a2-lacZ*^{floxed}*-Smad7* transgenic lines and transgenic lines expressing Cre under the control of the *Col11a2* regulatory sequences. By using these mice, we controlled the start of Smad7 overexpression at three steps of chondrocyte differentiation. We found that Smad7 overexpression exerts specific functions at multiple stages of chondrocyte differentiation. Smad7 overexpression in condensing mesenchymal cells inhibited their chondrocyte differentiation; Smad7 overexpression in round chondrocytes decreased proliferation; and Smad7 overexpression in flat chondrocytes inhibited maturation toward hypertrophy. *In situ* hybridization showed that Smad7 expression in chondrocytes was relatively low compared with that of the surrounding tissues during normal development.